VTT Technical Research Centre of Finland

Stress corrosion cracking initiation susceptibility of Alloy 182 with different surface treatments

Que, Zaiqing; Saario, Timo; Toivonen, Aki; Ehrnstén, Ulla

Stress corrosion cracking initiation susceptibility of Alloy 182 with different surface treatments

Z. Que [*], T. Saario, A. Toivonen, U. Ehrnstén

Nuclear Reactor Materials, VTT Technical Research Centre of Finland, Kivimiehentie 3, FI-02044, Finland

ABSTRACT

The effects of machining surface preparations on the stress corrosion cracking (SCC) susceptibility in boiling water reactor environment were evaluated for Alloy 182 weld metal. Constant extension rate tensile test, constant load test and electrochemical tests (passivation, current-voltage curves and electrochemical impedance spectroscopy) showed that the surface treatments strongly influence the resistance to SCC initiation. The machining-induced deformation and surface oxide layer from the surface treatments affect the re-passivation behaviour and SCC initiation susceptibility. The SCC susceptibility of the studied surface treatments was found following the sequence of shot peened > industrial surface milled > polished > advanced manufactured surface.

1. Introduction

Alloy 182 is commonly used as the weld filler metal between nickel-base alloys, low-alloy steels and austenitic stainless steels in nuclear power plants (NPPs) [1]. However, many cases where Alloy 182 suffered from primary water stress corrosion cracking (SCC) or environmentally-assisted cracking in the high-temperature light water reactor environments have been reported [2–7]. This issue has become one of the most critical safety concerns, which threatens the structural integrity and safe long-term operation of NPPs [8]. Surface machining inevitably results in heavily cold-worked surfaces, which could significantly influence the mechanical properties (yield stress and residual stress), microstructures (oxide layer, deformation and dislocation density) and enhance the SCC initiation of nickel-based alloys in the high-temperature water environments [5,9].

In NPPs, the components surfaces are rarely fine polished and are occasionally even coarsely ground, leading to a surface deformed layer that can significantly affect the crack initiation behaviour. Therefore, the effect of the surface finishing on the SCC initiation must be investigated carefully for finding the best practices for the nuclear industry [10]. The majority of work that were carried out in this field have been mainly focused on the measurement of SCC crack initiation time, crack growth rate and crack density resulting from the various surface treatments [11]. However, the preliminary conclusions were not consistent and have a huge discrepancy [12]. Scott et al. reported that the

electro-polished surface shown a lower SCC susceptibility than the mechanical-polished surface in pressurised water reactor (PWR) primary water since the sub-surface deformed layer can be removed by the electro-polishing treatment [3]. Similarly, Han et al. found that the electro-polishing can promote the formation of protective surface oxide scale, lead to the Cr enrichment at the grain boundary (GB) and enhance the SCC resistance of Alloy 182 in the primary PWR water environment [13]. In contradictory, Zhai reported that the electro-polished surface exhibited lower SCC resistance compared to the mechanically polished condition in PWR primary water [14] because the high-energy defects in the machining deformed surface layer can promote the diffusion of Cr towards the oxide layer, resulting in a compact oxide scale and thus enhance the SCC resistance in high-temperature water environment. Mendonça found that the protective oxide layer on ground surface is more homogenous than the polished surface [15]. The applied strain levels, the triaxial stress state, apparent contradiction and the detailed surface preparation process can be part of the reasons for the contradictory results of surface condition effect on SCC initiation. Surface treatments of light water reactor primary circuit components is considered as a potential way to mitigate SCC. However, to date there is insufficient (mechanical and electrochemical) data on the influence of surface finishing or treatment upon the SCC behaviour (particularly for early stages) for Alloy 182 and it is still not conclusive which surface treatment is efficient for reducing the SCC initiation susceptibility of Alloy 182 under light water reactor conditions [16].

Various SCC mechanisms, e.g. the cavity formation mechanism, the hydrogen-assisted SCC theory, the film rupture/slip dissolution mechanism, aging-related crystalline ordering and also the preferential intergranular (IG) selective oxidation mechanism [15,17–23] have been proposed for explaining the SCC behaviour in nickel-based alloys and stainless steels of the 300 series. However, SCC initiation mechanisms for Alloy 182 with different surface treatments in boiling water reactor (BWR) environments are still unclear. The influences of the machining-induced deformation, surface oxide layer microstructure, surface roughness and hardness from the surface treatments on the electrochemical passivation behaviour and SCC initiation susceptibility for the Alloy 182 are remained to be fully understood.

In this study, the effects of different surface treatments on the SCC initiation in Alloy 182 were investigated by the constant extension rate tensile test (CERT), constant load test and electrochemical tests (repassivation, current-voltage (CV) curves and electrochemical impedance spectroscopy (EIS)). The mechanisms of SCC initiation for the surface layer of Alloy 182 associated with different surface treatments in BWR environment were discussed.

2. Experimental

2.1. Material, roughness and hardness measurements

The investigated Alloy 182 was deposited at an Alloy 82-cladded low alloy steel plate. After deposition, post-weld heat treatment of 600 °C/ 15 min was performed. Optical emission spectrometry was used to analyse the chemical composition of the studied Alloy 182: 66.1% Ni, 14.6% Cr, 9.4% Fe, 6.31% Mn, 1.97% Nb, 0.59% Si, 0.25% Ti, 0.13% Mo and 0.032% C.

Four different surface treatments on Alloy 182 were investigated in this work. The reference surface (RS) was polished with a SiC P2000 grit paper. The Surface Advanced Machining (SAM) finish is a cryogenic face milling process. The Surface Treatment Industrial (STI) condition was flat milled. The Shot Peening (SP) finish was performed with ceramic balls over a ground surface, which is pre-treated with a SiC P80 grit paper. The details of these surface treatments can be found in [16].

The specimen surface roughness measurement was performed with 2D profilometry Mitutoyo Formtracer SV-C 3100 device and the measured roughness was verified with Form TalySurf Series 2 from TaylowHobson PNEUMO. The microhardness measurements of HV5 and HV0.1 on the specimen surface was performed with Durascan 80. The nanoindentation at the cross section (cut and machined along the loading axis) was carried out with Anton Paar, UNHT with Berkovich indenter and a maximal indentation depth of 80 nm (for allowing a small indentation spacing close to the surfaces).

2.2. Constant extension rate tensile test and constant load test

The studied and treated surfaces are in LT orientation and the expected orientation of SCC crack growth is in through thickness direction, S. Flat tapered specimens with 3 mm thickness, 10 mm maximum width and 6 mm minimum width along a gauge length of 20 mm were used for the CERT test and constant load test. It is worth noting that the flat tapered specimens have been developed and implemented to perform the screening of the EAC performance and feeding the modelling of the Alloy 182 with various surface treatments by our partners in EU projects (MICRIN+ and MEACTOS) [16,24,25]. For each specimen, one surface was with RS finish and the opposite face was with one of STI, SAM or SP finishes. The tests in high-temperature water were conducted with recirculating autoclaves. The crack initiation was monitored by the reversed direct current potential drop (DCPD) method.

CERT tests were performed with three specimens (RS/STI, RS/SAM and RS/SP) with a nominal strain rate of 1×10^{-7} s^{-1} (calculated from the average of the whole gauge length) in simulated BWR oxidising normal water chemistry (NWC) environment at 288 °C with 2 ppm

oxygen ($\sim$ +100 mV$_{SHE}$), a conductivity (inlet) of 0.05 μS/cm and a pH$_{288\ °C}$ of 5.7 [16]. The displacement-load curves of CERT tests were shown in Fig. 1. The ranking of the maximal load of the CERT tests are RS/SAM > RS/STI > RS/SP. The apparent SCC stress threshold was calculated by dividing the maximum load from the load-displacement curve by the critical cross-section area (determined from the thickness and the specimen width where the last SCC crack was found). A feature of using flat tapered samples is that the strain and the strain rate can vary over the gauge length. The amount of SCC cracks decreased over the gauge length from the smallest gauge section towards the largest section. This critical cross-section location with the last SCC crack is related to the critical stress under which no SCC will occur. The same CERT test with flat tapered specimens and evaluation procedure for assessing the SCC susceptibility have been applied in literatures [24,25]. The Ramberg-Osgood approximation [26] of the constitutive law fitting the stress-strain curve at 288 °C was applied for estimating the distribution of strain rate and strain along the gauge. When the specimen start to rupture, at the gauge where the last SCC crack was found, a strain rate of $\sim 2 \times 10^{-8}$ s^{-1} and a strain of 2% were estimated. The nominal strain rate is used in the article to simplify the discussion.

Constant load tests were performed to verify the results of CERT tests. For accelerating the SCC cracking, constant load tests in BWR NWC environment were performed with two specimens (RS/STI and RS/SAM) at testing temperature of 360 °C. Although temperature influences the stress relaxation, modulus and the crack growth rates of nickel-based alloys in primary water environments, no major changes in SCC initiation mechanism were foreseen with the increase of temperature from 288 to 360 °C. This is revealed by that the thermal activation energies for SCC initiation were insensitive to the change of temperatures in this range [27–29]. Based on the CERT results, stress level for the minimum cross-section was set to 407 MPa. It was expected that at the increased temperature, crack would initiate quick and could be detected by the DCPD method. However, no cracking was detected with DCPD within the first $\sim$ 1000 h exposure. After an intermediate scanning electron microscopy (SEM) inspection, the specimens were put back to autoclave. The stress level was then increased incrementally. A reasonably long period ($\sim$ 1000 h) for crack initiation before new higher stress level was applied. Stepwise increasing of the stress level was done using a strain rate of 1×10^{-7} s^{-1}. As no cracking was detected by the DCPD method at any point of the exposures, the specimens were taken out for final SEM inspection after $\sim$ 3200 h total exposure time at 407–440 MPa stress levels. It is worth noting that there was no flat tapered RS/SP specimen available for the constant load test but electrochemical tests were
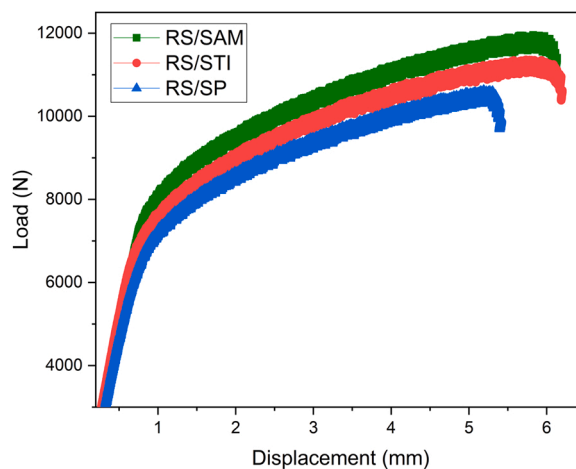

Fig. 1. Displacement-Load curves of the CERT tests with flat tapered specimens with RS/SAM, RS/STI and RS/SP surfaces tested in simulated BWR NWC environment at 288 °C. The ranking of the maximal load of the tests: RS/SAM > RS/STI > RS/SP.

performed for SP and RS surfaces instead.

2.3. Electrochemical tests at T = 288 °C

Normal BWR water has a very low conductivity, and thus electrochemical measurements (which depend on current flowing in the electrolyte/water) are virtually impossible. To overcome this, the conductivity needs to be increased with addition of e.g. sulphate (as Na_2SO_4). The high temperature passivation tests were performed in an AISI 316 L stainless steel autoclave that is attached to a recirculating loop.

High temperature passivation tests on RS and SP surfaces were performed at T = 288 °C. The measurements were performed in a representative BWR crevice solution, i.e., 100 ppm SO_4^{2-} (added as Na_2SO_4), simulating the crevice/crack tip chemistry at an already initiated crack tip (of 1–3 mm depth) [30]. Oxygen was removed by N_2-bubbling (since in the crevice/crack tip there is no oxygen). A measurement wire was welded onto the side of the specimens. The SP sample was covered with several layers of PTFE tape except for the shot peened surface. The re-passivation rate was measured with Ivium CompactStat potentiostat by first polarising the sample to -0.65 V_{SHE} for a minimum of 600 s and then stepwise increasing the potential to the desired re-passivation potential ($+0.15$ or $+0.25$ V_{SHE}), at which the current was followed for 7.5 s with a measurement interval of 1 ms. The re-passivation potentials chosen, $+0.15$ and $+0.25$ V_{SHE}, were selected based on the open circuit potential measured during the CERT tests, and reside in the stability area of $NiO*Fe_2O_3$, as shown in Fig. 2. As seen in Fig. 2, the base potential of -0.65 V_{SHE} (at which the specimen potential was residing before the re-passivation) is about 0.05 V below the hydrogen line. At this potential, NiO is expected to reduce to Ni, with no hydrogen generation due to water reduction.

In addition to the re-passivation tests, the RS and SP surfaces were characterised using standard CV curves (with sweep rate of 1 mV/s) and EIS at -0.47 V_{SHE} (E_{oc}) and $+0.15$ V_{SHE}.

2.4. Materials characterisation

The specimens were sectioned parallel to the loading direction with a mechanical blade saw, then mounted in a conductive resin, before being mechanically ground and polished with a 0.25 μm diamond paste. The final surface preparation was with a non-crystallising amorphous colloidal silica suspension (0.04 μm). The specimens were characterised using SEM and plasma focused ion beam (PFIB). A Zeiss Crossbeam 540

Fig. 2. Pourbaix-diagram for Alloy 182 (Ni-Cr-Fe-H_2O system) at T = 288 °C and molar concentration of the metals in water at 10^{-6} M. The blue rectangle depicts the starting potential for re-passivation measurements and the red spots the potentials to which the potential was stepped and at which the re-passivation current density was monitored as a function of time.

equipped with a solid-state four-quadrant backscatter detector (BSD) and an EDAX Hikari Plus electron backscatter diffraction (EBSD) detector was used. The near-surface microstructure was investigated using SEM secondary electron (SE) and backscatter electron (BSE) imaging techniques. BSE imaging was conducted at an accelerating voltage of 20 keV with a working distance (WD) of 4–7 mm. EBSD mapping was conducted at an accelerating voltage of 15 keV and WD of 12–15 mm with 70° tilting and a probe current of 1.5 nA. EBSD inversed pole figure (IPF) images were analysed by TSL OIM Analysis 8 software. Inclusion analysis was performed with SEM-Energy Dispersive X-Ray (EDX). For reducing the interaction volume of the incident electrons with the material and generate EDX data mainly from the inclusion itself, EDX with an accelerating voltage of 5–10 keV and a probe current of 1.5 nA was applied.

3. Results

3.1. Baseline characterisations

The SEM images of the specimen surfaces with the four finishes are shown in Fig. 3. RS surface is free of clearly oriented manufacturing marks (the polishing was performed parallel to the loading axis). SAM surface has site-specific machining marks, which result from the face milling process and depend on the mill tool-specimen respective position. STI surface has parallel machining marks with a ~ 60° angle from the loading axis. SP surface has a typical peening feature with pits induced by the ceramic balls. Some defect cracks or flaws are present on the SP surface.

The summary of surface roughness and microhardness measurement is presented in Table 1. In good accordance with the observation of the surface conditions in Fig. 3, the surface roughness follows the sequence of SP > SAM > STI > RS. SAM has a high surface roughness deviation due to the fact that the face milling site-specific machining marks heavily depend on the tool location. The SP surface has a high variation in HV5 measurements due to its high surface roughness. With a smaller load and indentation depth, HV0.1 is more sensitive in sensing the hardness difference between surface treatments than HV5 for RS, STI and SAM surfaces. However, no reliable HV0.1 results could be obtained from SP surface due to the large amount of surface pits induced by the ceramic balls. The surface microhardness follows the sequence of SP > SAM > STI > RS, showing good correlation with that of the surface roughness. The surface roughness and the surface microhardness indicate the deformation level from the surface machining processes.

Fig. 4 shows the representative near-surface microstructures of oxide layer after testing in BWR NWC high-temperature water at 288 °C as function of the surface finishes. An inhomogeneous oxide layer of ~ 200 nm was observed for RS surface. The STI surface showed a homogeneous ~ 350 nm thick oxide layer. The SAM surface had ~ 600 nm uniform and compact oxide layer. SP surface had a cracked oxide layer of ~ 500 nm and its thickness varied from different locations. Fig. 4 also reveals the influence of the different machining processes on the deformation layer. A very limited deformation with a ~ 400 nm thick ultrafine-grained (UFG) and deformed layers beneath the oxide layer of the RS surface finish was found. STI machined specimen showed a 2-layer deformation. Specifically, the first layer was the ~ 3–4 μm UFG layer and the second layer had the presence of deformation bands that extended ~ 10–15 μm into the matrix. For the SAM surface, ~ 5 μm UFG layer and ~ 15 μm complex deformed structure were observed. The SP surface shown a 2-layer machining-induced deformation structure, with highly variable UFG layer extending ~ 3–5 μm and an underneath deformation layer with a depth of ~ 60 μm. Some deformation bands were observed more than 100 μm from the SP surface finish. The summary of near-surface microstructure from different surface treatments is presented in Table 1.

Fig. 5(a) shows the cross-sectional nanohardness as a function of distance to the machined surface. The nanohardness decreases from
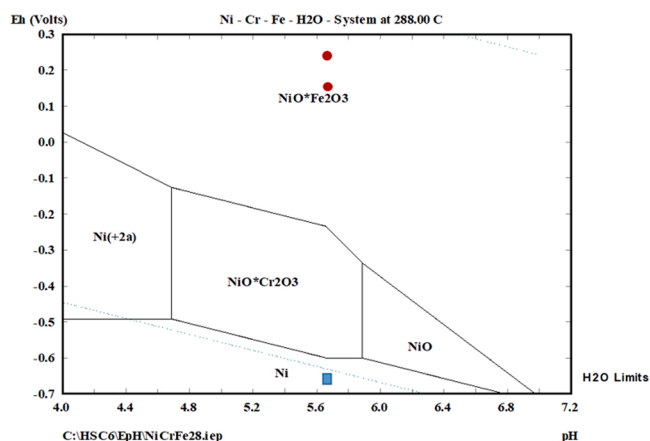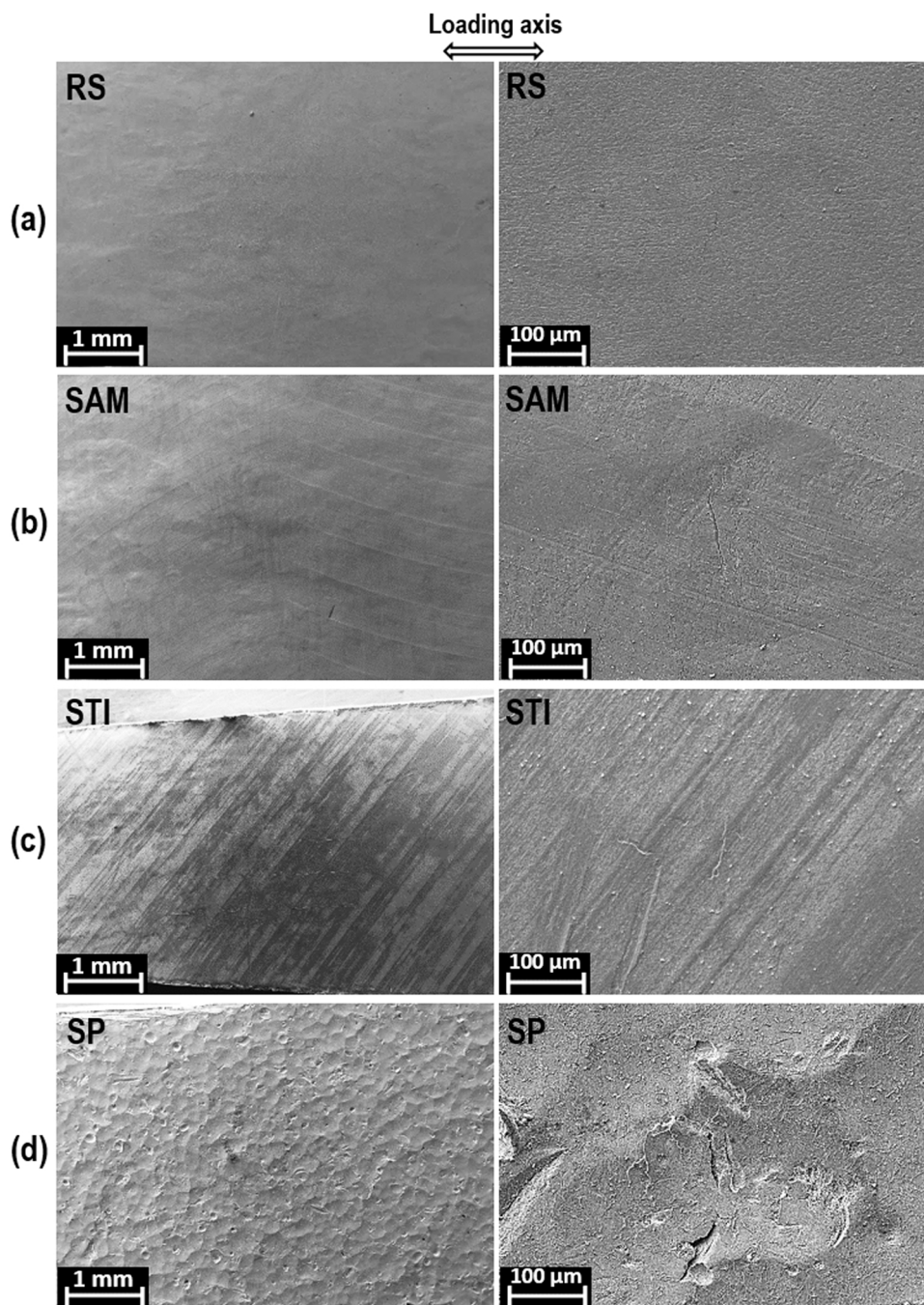
Fig. 3. Specimen surface with the various treatments. (a) RS; (b) SAM; (c) STI and (d) SP surface.

surface to the bulk of the Alloy 182 material of ∼ 4–4.5 GPa over 5–15 μm with RS, STI and SAM surfaces whereas the nanohardness is still around ∼ 6 GPa over ∼ 50 μm with SP surface. The nanohardness at 1 μm from the surface is in the sequence of SP > SAM > STI > RS. The nanohardness and indentation load (with constant max indentation depth of 80 nm) at 10 μm from the surface (Fig. 5(b)) are in the sequence of SP > SAM > STI > RS, which confirms the cross-sectional charac-terisation results of the machining deformation and correlates well with the HV0.1 surface microhardness ranking. It is worth noting that a slightly deeper machining deformation seems to be revealed by the cross-sectional nanohardness measurement (Fig. 5(a)) than the SEM-BSE characterisation (Fig. 4), particularly for RS surface. It was probably due to the high sensitiveness to the edge flatness of the specimen by using a maximal indentation depth of 80 nm in nanoindentation, since very

similar thickness of UFG and deformed layers beneath the RS finish as in the SEM-BSE characterisation was reported from our previous TEM/TKD analysis [16].

3.2. Constant extension rate tensile test and constant load test

CERT tests were used to examine and compare the SCC susceptibility as function of surface preparations in a reasonable time frame. Table 1 shows the apparent SCC initiation threshold stress as a function of sur-face treatments. The apparent SCC initiation threshold stress was found to follow the sequence (from highest to lowest) of SAM > RS > STI > SP, which indicates a lowest SCC resistance of SP. This corresponds well to the ranking of maximal load for the CERT tests in Fig. 1.

Fig. 6 shows the SEM-BSE images of crack tips from specimens with

Table 1
Summary of roughness, surface microhardness, microstructure and apparent SCC threshold stress from the machined surfaces.

Machined surface	Roughness (Perpendicular to loading axis)		Microhardness (on surface)		Microstructure (cross-sectional)		Apparent SCC threshold stress (at 288 °C with a nominal strain rate of 1×10^{-7} s^{-1})			
	Avg. R$_a$ (μm)	Avg. R$_z$ (μm)	HV5	HV0.1	Inner oxide layer	Manufacturing deformation layer	Maximum load (N)	Crit. width, thickness and area (mm, mm, mm²)	The estimated local strain rate (s^{-1}) in BWR NWC	Threshold stress (MPa)
SAM	0.4 ± 0.2	2.3 ± 1.1	266 ± 13	422 ± 15	Uniform ~ 600 nm	UFG layer of ~ 5 μm Deformed layer of > 15 μm	11,760	8.28, 3.08, 25.50	~ 2.1 × 10⁻⁸	461 ± 14
STI	0.25 ± 0.03	1.4 ± 0.3	247 ± 7	361 ± 14	~ 350 nm	UFG layer of ~ 3–4 μm Deformed layer of 10–15 μm	11,200	9.42, 3.15, 29.67	~ 1.5 × 10⁻⁸	378 ± 13
SP	2.4 ± 0.3	18.9 ± 3.6	408 ± 48	–	Cracked ~ 500 nm	UFG layer of ~ 3–5 μm Deformed layer of > 100 μm	10,500	9.43, 3.07, 28.95	~ 1.5 × 10⁻⁸	363 ± 17
RS	0.05 ± 0.003	0.4 ± 0.05	228 ± 6	272 ± 6	~ 200 nm	> 400 nm	–	–	~ 1.8 × 10⁻⁸	~ 410 ± 9 (average of the 3 specimens)

different surface treatments. With RS surface, an IG SCC with cracking along the GB was observed. For SAM, STI and SP surfaces, transgranular (TG) SCC cracks with slip bands ahead of the crack tips were observed.

Representative IG SCC cracks (with depth of ~ 6 μm) were analysed from RS surface, as shown in Fig. 7(a, b). The formation of voids was observed along the GB in Fig. 7(c). The crack propagated by linking to voids resulted from the deformed and fractured inclusions. In Fig. 7(d), EDX revealed that the fractured inclusion particle was mainly consisted of Nb-rich carbides and Si-rich oxides. Fig. 7(e, f) exhibits IG selective oxidation by the oxidation along the GB ahead of the SCC crack tip.

SE image, SEM-BSE and EDX maps revealing TG SCC crack with STI surface were shown in Fig. 8(a, b). Oxidation and dissolution along the slip bands ahead of the crack tip was observed. Discontinuous TG crack growth with crack arrest and blunting were also found. 3D reconstruction of SCC crack from STI surface by slice and view (slice of 200–300 nm) using PFIB is shown in Fig. 8(c, d). The SEM images of the crack were filtered, aligned and 3D reconstructed. Rotary images of reconstructed 3D TG SCC crack reveals the complex crack morphology and structure. The SCC crack opening is ~ 1–5 μm. The main crack growth plane appears to be perpendicular to the loading axis. The SCC crack propagates in the depth and width direction of 20 and 15 μm, respectively. As the crack progresses into the material, it becomes less planar, stretching itself accommodating to the stress distribution.

For verification of the surface finish effects on the SCC susceptibility, constant load test at different stress levels were performed (Fig. 9). A few SCC cracks were found on the STI surface after the first 1000 h exposure at 407 MPa. More SCC cracks were observed on the STI surface after the second exposure ending with the 440 MPa stress level. The SCC cracks identified on the STI surface were found to be parallel to the machining marks by the flat milling process. No SCC cracking was found on the RS surface after the first 1000 h exposure at the stress level of 407 MPa. However, SCC cracks were observed on the RS surface after the second exposure ending with the stress level of 440 MPa. The same SCC behaviour on the RS surfaces was observed for both specimens. No SCC cracking was found on the SAM surface even after the second exposure ending with the 440 MPa stress level. With the constant load test in BWR NWC water at 360 °C, the observed SCC resistance (from highest to lowest) ranks as: SAM > RS > STI, which is in good accordance with the CERT test results.

3.3. Electrochemical behaviour

3.3.1. Voltammograms (CV) and electrochemical impedance spectroscopy (EIS)

It is worth noting that the results presented in this section are based on the nominal surface areas of the specimens. The ratio between the nominal and real surface area, which takes into account the surface morphology, may be slightly different for the two surface conditions studied (RS and SP) since the surface roughness of the specimens in these two conditions is slightly different. However, the small difference in the surface area has a very limited influence on the comparison of the electrochemical behaviours of RS and SP surfaces.

A comparison of the current density - potential curves for RS and SP surface conditions is shown in Fig. 10. The SP surface shows a much higher current density at the anodic potential range compared to RS surface, indicating an electrochemically more active surface. The EIS spectra at corrosion potential (E$_{oc}$ = −0.47 V$_{SHE}$) and at E = +0.15 V$_{SHE}$ shown in Fig. 11 indicate that the SP surface has a clearly higher corrosion rate, evidenced by the impedance magnitude at the low frequency end of the spectra being clearly lower for the SP surface than RS surface.

3.3.2. Re-passivation

The current density – time curves of the RS and SP surfaces shown in Fig. 12 for two potentials (the specimen potential was stepped from −0.65 V$_{SHE}$ to +0.15 or +0.25 V$_{SHE}$) show that the re-passivation is
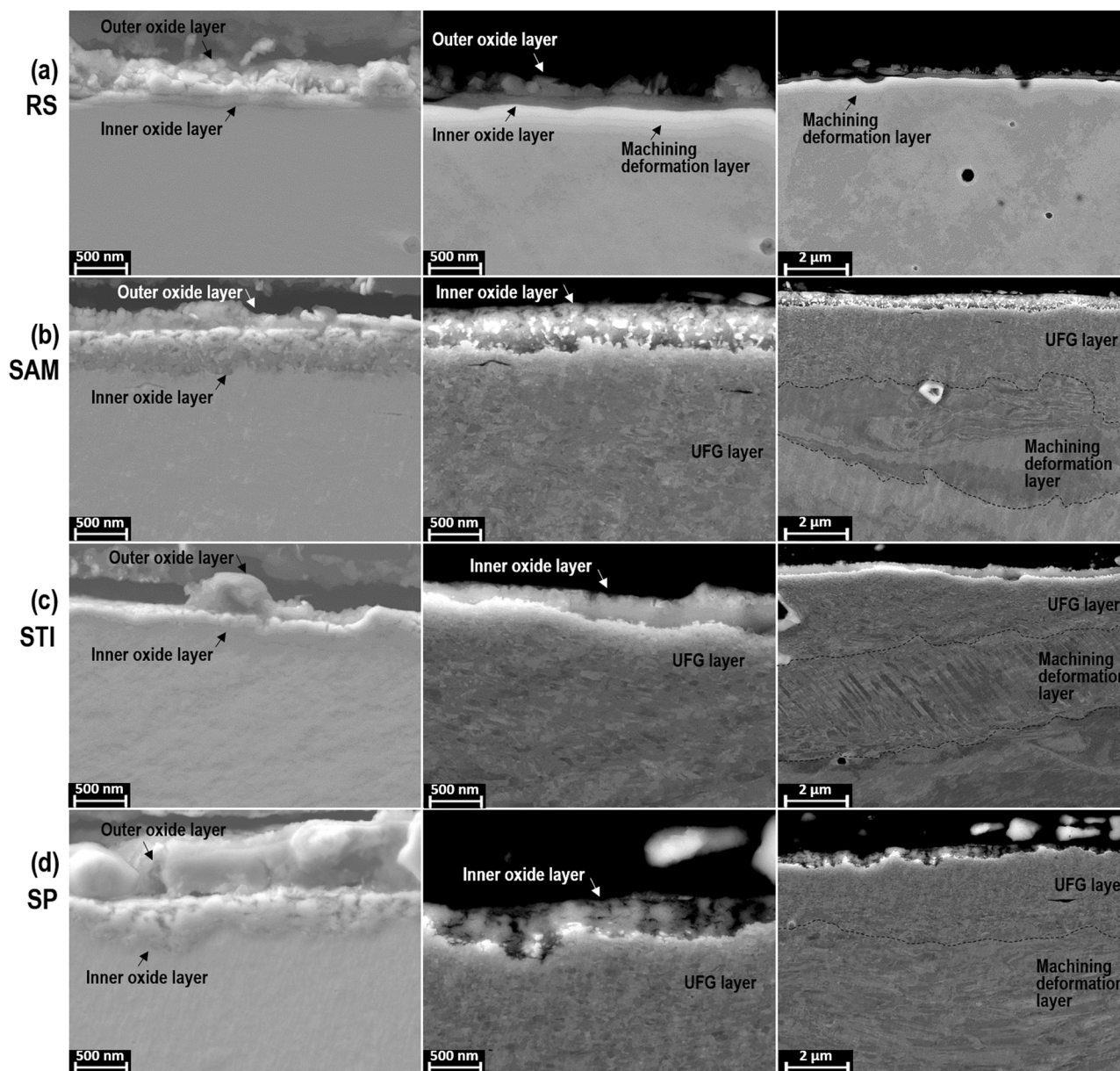
Fig. 4. SEM-SE images of oxide layer and SEM-BSE images of machining-induced deformation microstructure from cross-sections of specimens with different surface treatments. (a) RS; (b) SAM; (c) STI and (d) SP surface. Tested in BWR NWC water at 288 °C.

more efficient for the RS surface. The current density peaks are several times higher for the SP surface than for the RS surface, and the current density level at the end of the 7.5 s measurement period is much higher for the SP than for the RS surface. The high-temperature electrochemical re-passivation, CV curves and EIS tests show the same conclusion that SP surface is more susceptible to corrosion in high-temperature water.

4. Discussions

In this study, CERT, constant load test and electrochemical measurements were applied for investigating the SCC initiation susceptibility of Alloy 182 with surface treatments of RS, SAM, STI and SP. Though it is known that the accelerated CERT test with dynamic plastic loading is not the best approach for determining the SCC initiation threshold stress in a nuclear component relevant condition [24], CERT tests are suitable for screening and can provide the general comparison of SCC initiation susceptibility within a reasonable time frame [18]. The results of CERT tests were verified by the constant load tests. The

electrochemical tests including re-passivation, CV and EIS tests allow a comprehensive understanding of the electrochemical processes and behaviours of the RS and SP surfaces. To sum up, the SCC susceptibility of surface treatments were investigated via the static electrochemical polarisation/passivation/impedance measurements without loading (by high-temperature electrochemical tests), the constant load tests and the dynamic loading tests (by CERT tests) in this study.

4.1. Effect of surface microstructure on SCC initiation

The surface roughness (also the surface conditions including machining marks and flaws) and hardness, surface oxide layer microstructure and machining-induced deformation of the surface treatments have significant effects on the SCC initiation susceptibility, as revealed by the characterisations and tests.

Surface state: As shown in Fig. 9(b), the SCC cracks observed on the STI surface were found parallel to the machining marks resulting from flat milling process. The STI surface had a higher surface roughness
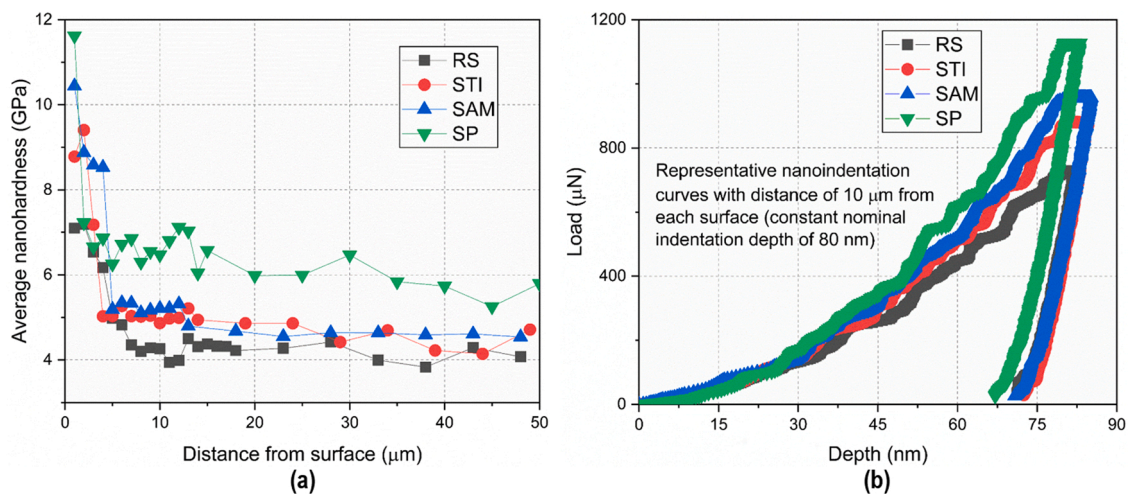
Fig. 5. (a) Average cross-sectional nanohardness as a function of distance from each surface finish; (b) Representative cross-sectional nanoindentation depth-load curves with distance of 10 μm from each surface.
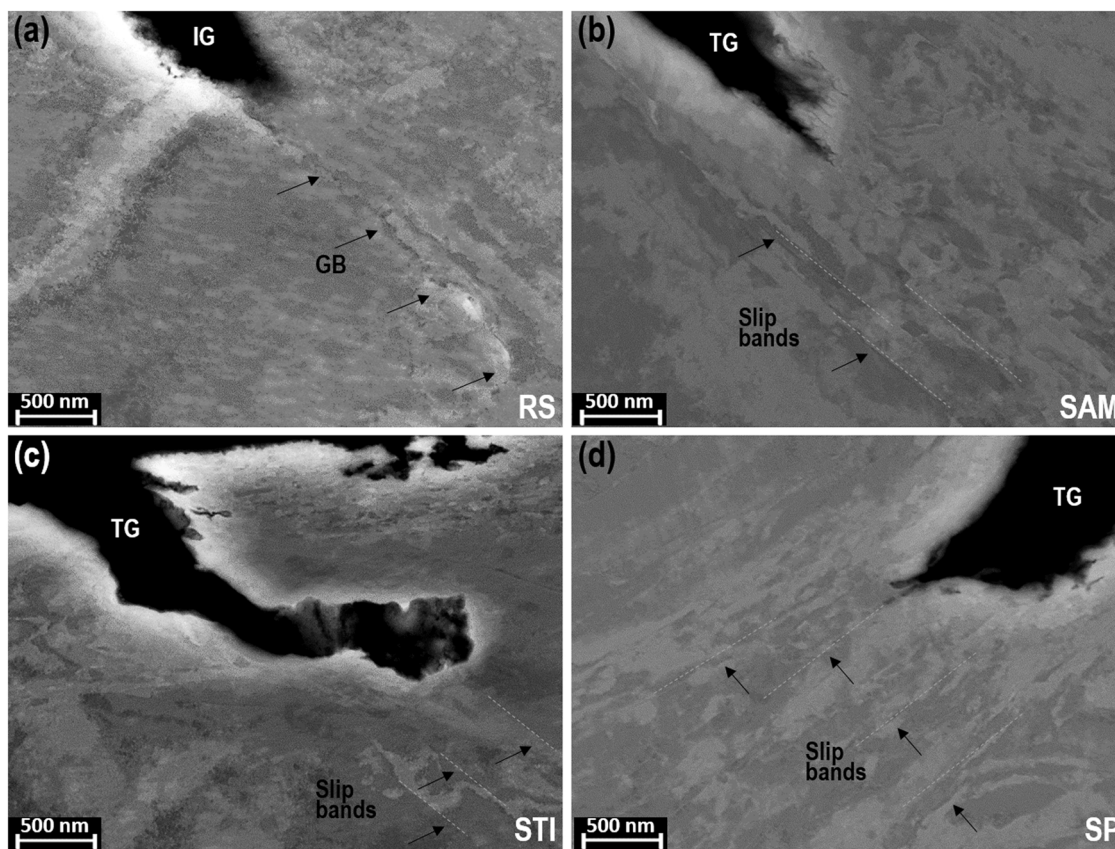

Fig. 6. SEM-BSE images of crack tips from cross-sections of specimens with different surface treatments. (a) RS; (b) SAM; (c) STI and (d) SP surface.

compared to the RS surface finish, and the grinding marks could become preferential SCC crack initiation sites due to notch and hardening effects, particularly when the surface grinding marks coincide with the GBs of the UFG or deformed layer [31]. The SP process with ceramic balls resulted in large amount of surface defects/pits (Fig. 3(d)) and deteriorated the SCC resistance.

Oxide film and deformation layer: The growth behaviour and microstructure of surface oxide layer is mainly controlled by the oxidation process and has no direct relation to the residual strain profile underneath the surface layer [32]. The surface oxide layer exhibits a

higher Young's modulus and a lower ductility compared to the substrate matrix [33]. The surface oxide layer also act as the isolation layer between the material matrix and the high-temperature water environment, which slows down the diffusion process and dissolution and thus influence the cracking initiation [34]. The SCC initiation process has a direct relationship to the inward oxidation penetrating the oxide layer to the matrix GBs in the form of preferential IG corrosion (RS surface) or along slip bands as slip dissolution-oxidation (SAM, STI and SP surfaces). Consequently, the compact and homogeneous SAM oxide layer can better retard the preferential oxidation and thus has less preferential
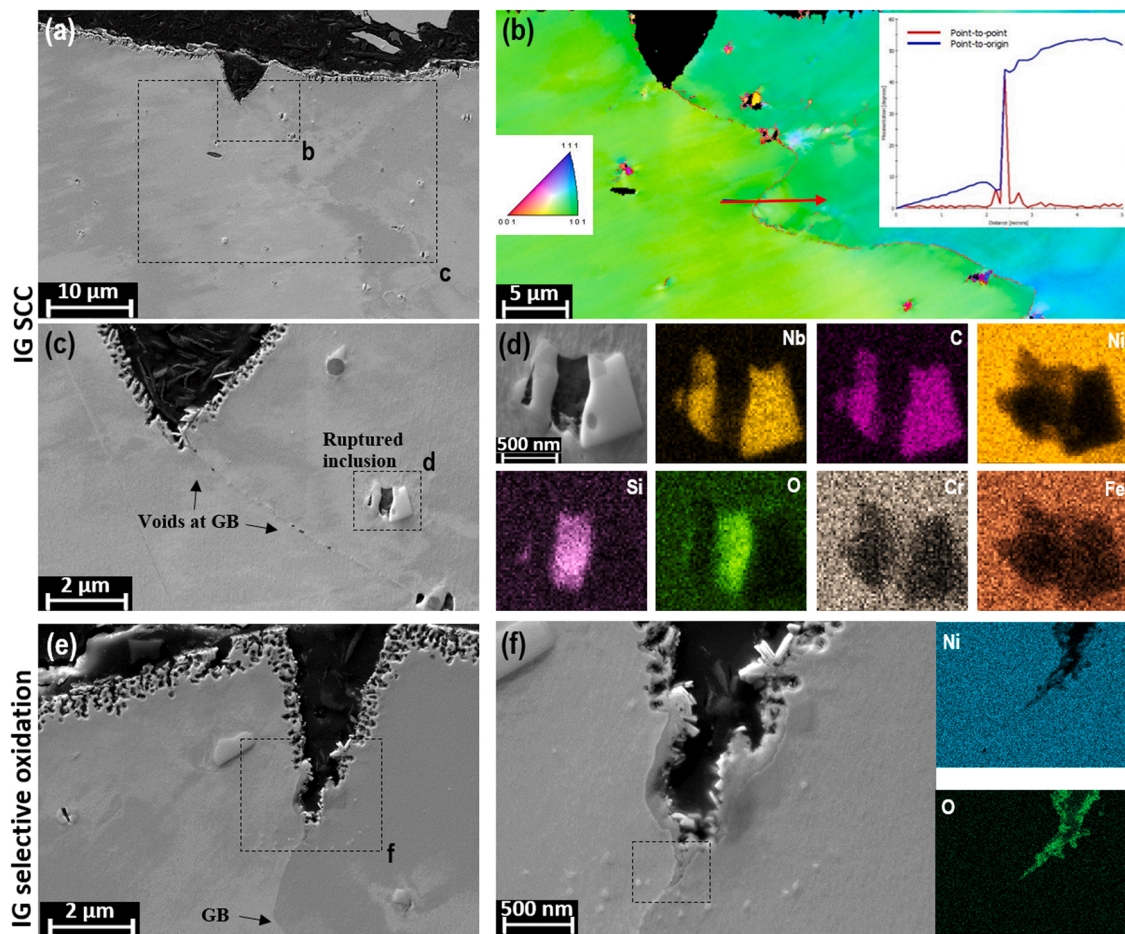
Fig. 7. (a, c, e, f) SE image, (b) EBSD IPF and (d, f) SEM-EDX maps showing ruptured inclusions and IG SCC crack with RS surface.

nucleation sites for local cracking than the SP surface with cracked oxide film. A potential reason for the thicker and more uniform oxide layer in the SAM surface than the other surface finishes can be associated with the higher element diffusivity in the UFG nano-crystalline layer compared to a coarse-grained region based on the lower activation energy required for diffusion in the deformed grains and the much higher fraction of GBs in volume. The cracked oxide film of the SP surface may result from the surface defects or the severe machining induced deformation. The oxide film of the SP surface exhibits a high porosity and can be less protective in resisting the SCC initiation [10].

Another critical factor that significantly influences the SCC initiation is the elemental diffusivities (e.g. Cr and O) in the deformed microstructure [35]. The machining-induced UFG layer and deformation bands with accumulated dislocations in the near-surface area can promote the stress-assisted diffusion and oxidation [36]. The dislocation density in the deformed layer (the UFG layer and at the deformation bands) is much higher compared with the intact matrix. Dissolution along the slip bands can also promote micro-crack initiation through a crevice corrosion effect. Saravanan suggested that a threshold value for the local dislocation density is required to generate the stress required for an oxidised GB to fail (for SCC initiation) [37]. The SCC initiation susceptibility is strongly dependent on both GB chemistry and misorientation. Cracking takes place preferentially at high-energy structures like high-angle GBs (HAGB) with highly-disordered boundary and deformation bands with high density of dislocations [38]. Random HAGBs result in fast Cr diffusion and GB migration and thus show low SCC resistance [39].

SCC mechanisms: For RS surface, SCC crack grown along GBs after preferential IG oxidation (Fig. 7(e, f)). IG crack propagation occurred

when the initiated SCC cracks grown to the matrix GBs under external stress. Void formation was observed along the GB in Fig. 7(c). These voids may have a central role providing an easy pathway towards the next cracked inclusion further along the GB since Nb-rich carbides and Si-rich oxides (Fig. 7(d)) are the preferential sites for void formation and growth. A direct correlation between cavity density and crack growth was observed [40,41]. The strain localisation at the inclusions (particularly the IG inclusions) may also induce the preferentially propagation of SCC. In addition to the similar effects on void generation and strain localisation, it is worth to note that there might be a different role of carbides and oxides on SCC initiation. GB carbide may in addition promote crack blunting by being the dislocation source and the material could passivate faster in the presence of GB carbide [42]. The dominating SCC initiation and propagation mechanism for the RS surface in this study is an IG selective oxidation mechanism, which is further assisted by the voids and fractured inclusions along the GB.

For SAM, STI and SP surfaces, the SCC initiation mechanism is a slip dissolution-oxidation mechanism. After the rupture of protective passivation films by the slip bands ahead of the crack tip, the fresh nickel-based alloy is exposed to the high-temperature water environment and the oxides is formed and repassivation occurs again. The repeating of this process under the external stress will lead to a discontinuous crack growth with crack arrest events.

The SCC behaviour of the SP specimen is in good accordance with the previous study [16], which suggested that SP may not be efficient in mitigating SCC in NPP primary high-temperature environments, contradictory to the finding that other surface peening methods such as laser peening and water jet techniques can be effective [43]. This study showed the data from surface roughness, surface and cross-sectional
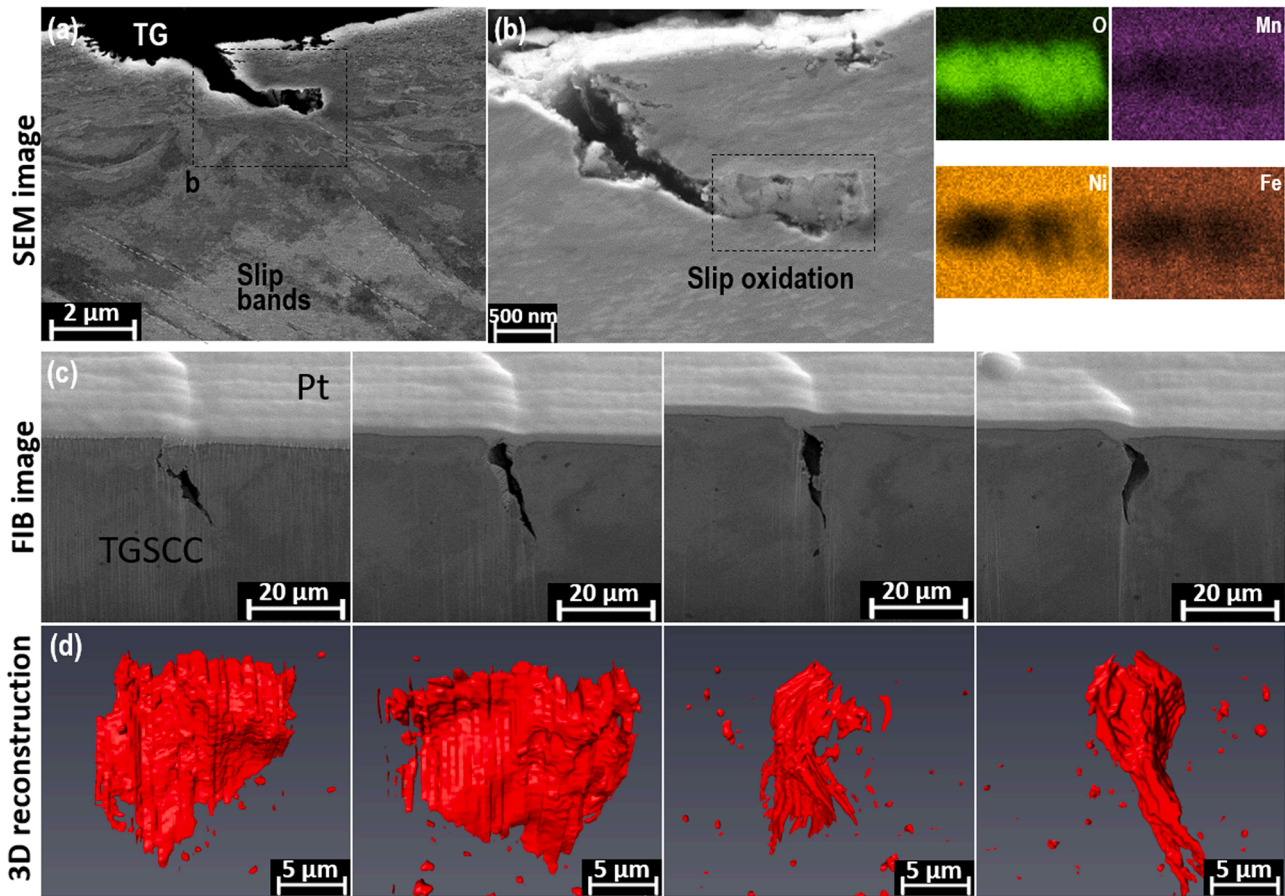
Fig. 8. (a) SE image and (b) SEM-BSE and EDX maps showing TG SCC crack with STI surface; (c) Slice and view and (d) 3D reconstruction of TG SCC crack from specimen with STI surface.

hardness and the cross-sectional microstructural evidences, which clearly indicate the severity of damage due to the SP process.

4.2. Electrochemical behaviour

The SCC of Alloy 182 involves an incubation stage by electrochemical process, followed by a slow propagation period with SCC crack length smaller than a critical size and a rapid cracking stage resulting into fracture in the end [44,45]. Mechanical treatments on surface can enhance electro-chemical activity of the surface, which significantly influence the SCC susceptibility [46]. The investigation of electrochemical behaviour/response from RS and SP surfaces can thus assist in the understanding of the initiation susceptibility.

In the range of re-passivation rate where SCC may occur, the charge spent in forming a new surface film, Q_f, is related to the crack growth rate (CGR) through Eq. (1) [20]. Each re-passivation event leads to a decay in current density with time. Q_f can be estimated with the area under the current density - time curve (hatched area).

$$CGR = \frac{M}{z\rho F} \cdot \frac{Q_f}{\varepsilon_f} \cdot \frac{d\varepsilon_{ct}}{dt} \tag{1}$$

where M = atomic weight of the dissolving metal, z = number of electrons transferred in the oxidation reaction, ρ = density of the metal, F = Faraday's constant, ε_f = fracture strain of the surface film and $d\varepsilon_{ct}/dt$ = crack tip strain rate. The charge density, Q_f, can be calculated as

$$Q_f(t) = \frac{\int_0^t (I_t - I_p) dt}{A} \tag{2}$$

where I_p is the passive current density at the potential in question, I_t the

time dependent current after the film breaks and A the surface area of the specimen. The passivation during the initial stage follows the place-exchange model, where $log (I_t)$ is linearly proportional to $Q_f(t)$

$$\log(I_t) = \log(k') + \beta V - \frac{Q_f(t)}{K} \tag{3}$$

After the short initial stage, the passivation proceeds by the high field ion conduction model, where $log (I_t)$ is linearly proportional to $1/Q_f(t)$

$$\log(I_t) = logA + \frac{cBV}{Q_f(t)} \tag{4}$$

in which k', K, β and c are constants, A and B the constants for the activation energy of ion migration in the film and V the applied potential. Since the high-field ion conduction stage of the re-passivation event determines the protectiveness and the stability of the resulting film, the parameter cBV, determined from the re-passivation current measured as a function of time, can be used as a parameter to study materials susceptibility to SCC.

The charge density $Q_f(t)$ in Eqs. (3) and (4) above can be calculated by integrating the current density-time curves shown in Fig. 12. The cBV parameter can then be extracted as the slope of the current density vs. Q_f $(t)^{-1}$ curve, Fig. 13. The higher the cBV-value, the slower the re-passivation rate [47]. A high re-passivation rate results in a low susceptibility to SCC due to the low amount of dissolution, whereas a low re-passivation rate typically results in SCC due to high amount of dissolution. The cBV parameters of duplex stainless steel measured by Bernard et al. [47] were below 10 in the potential range where no SCC was found and between 10 and 25 in the potential range where SCC was found, thus quite comparable to those calculated in this study. This tends
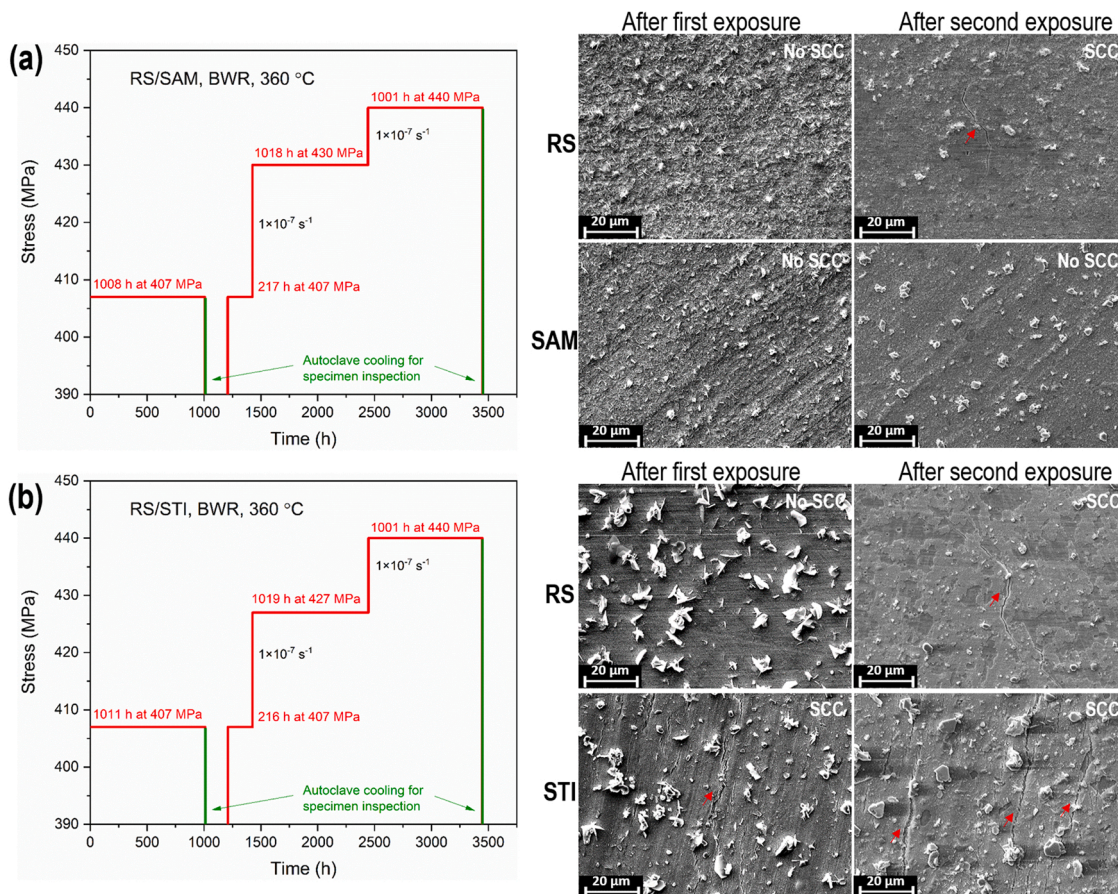
Fig. 9. Constant load test with specimens of (a) RS/SAM and (b) RS/STI surfaces in BWR NWC water at 360 °C.
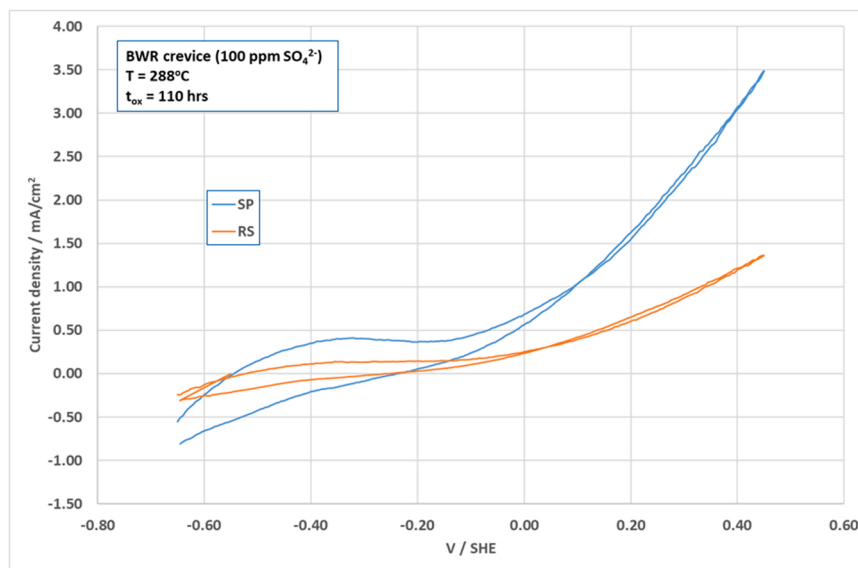

Fig. 10. Comparison of voltammograms (1 mV/s) for RS and SP surfaces.

to indicate that the SP surface is more susceptible to SCC while the RS surface is not, in line with the CERT results in the present work.

4.3. Shot peened surface

Normally peening is identified as an effective method for mitigating SCC initiation [42,46,48,49] since peening can introduce the

compressive residual stress state. However, in this work the specimens with the SP surface finish presented the highest SCC susceptibility among all the studied surface finishes. Some might claim that the CERT test is aggressive with dynamic straining and will result in the complete relaxation of residual stress [50] induced by the SP process. When the compressive residual stress is relaxed, surface defects induced by peening and the plastically deformed layer enhance SCC initiation and
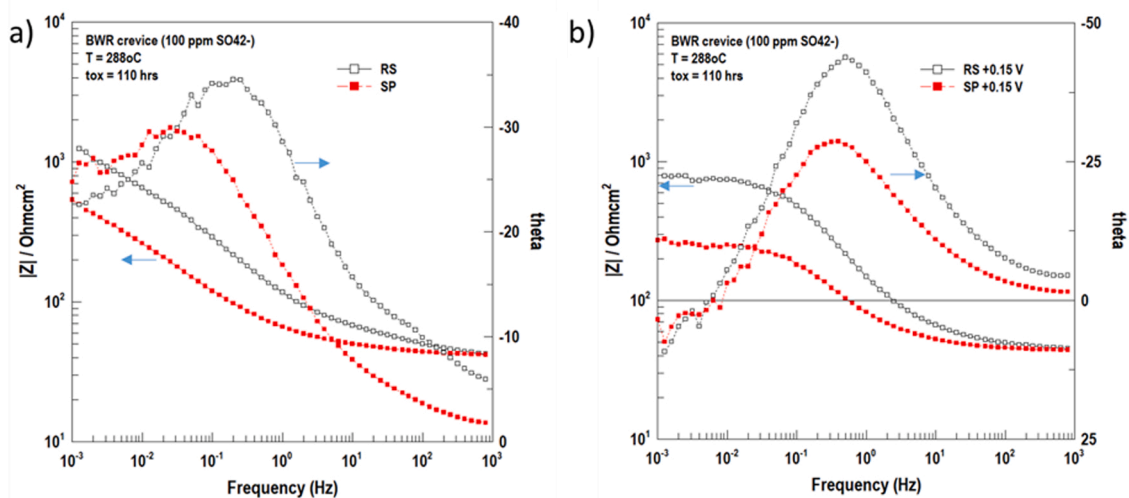
Fig. 11. Impedance magnitude /Z/ and phase angle as a function of frequency for RS and SP surfaces at (a) corrosion potential ($E_{oc} = -0.47$ V_{SHE}) and (b) at E = +0.15 V_{SHE}.
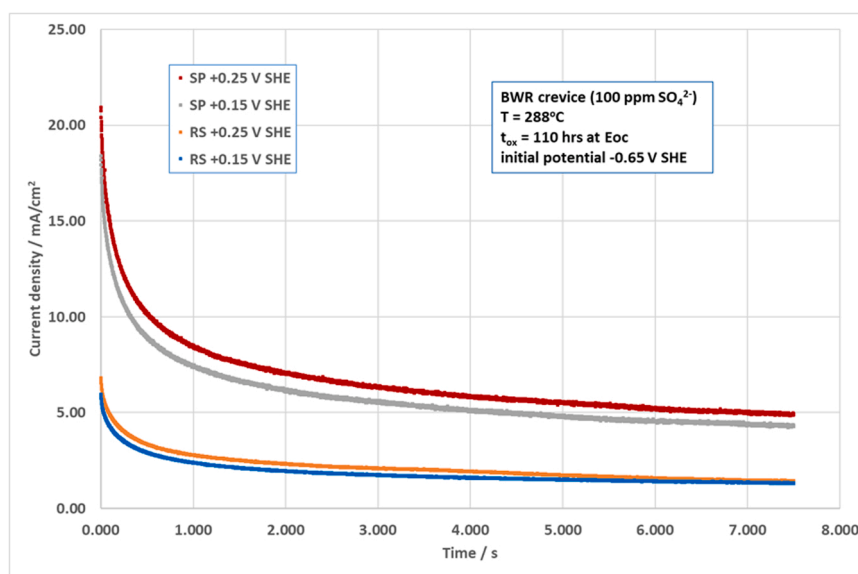

Fig. 12. Comparison of re-passivation behaviour of RS and SP surfaces. The specimen potential was stepped from -0.65 V_{SHE} to +0.15 or +0.25 V_{SHE}.

result in the low SCC resistance of the SP surface. The authors are aware of the potential drawbacks of applying CERT technique to evaluate the SP effect on SCC.

However, interestingly, the high temperature re-passivation tests (corroborated by the CV and EIS data) confirmed the observation that RS surface shows a clearly lower current density and better re-passivation than the SP surface even though the re-passivation specimens were not subject to loading at all and thus the compressive residual stress in SP surface would not be relaxed. The electrochemical tests emphasise the important role of surface microstructure in addition to the residual stress profile on SCC for the SP surface. Boursier reported that one side SP specimen had a reduced SCC initiation time [51], which is in good accordance with the results shown in this work. A general suggestion on applying the peening techniques for mitigating the SCC initiation of nuclear components is that the peened surface will need to be carefully monitored to avoid potential flaws or defects.

5. Conclusions

The effect of four different surface treatments on the SCC initiation susceptibility in Alloy 182 was investigated in simulated BWR NWC high-temperature water environment using CERT, constant load and electrochemical tests.

- The surface roughness, microhardness and cross-sectional nano-hardness follows as (from highest to lowest) SP > SAM > STI > RS.
- The CERT technique permits a qualitative comparison of the surface treatments. The apparent SCC initiation threshold stress followed the sequence of SAM > RS > STI > SP.
- The constant load test in BWR NWC environment at 360 °C rank the SCC resistance as: SAM > RS > STI.
- The dominant mechanism of SCC cracking of Alloy 182 with RS surface in BWR NWC is IG selective oxidation mechanism, assisted by the void formation along the GB.
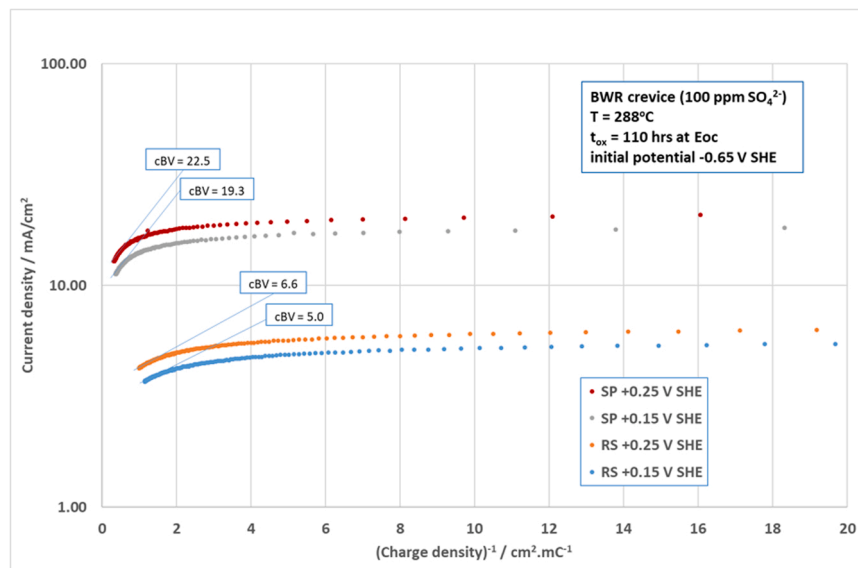
Fig. 13. Current density vs. (charge density)$^{-1}$ for SP and RS surfaces at E = +0.15 and +0.25 V$_{SHE}$. Data up to 100 ms was used for the cBV-analysis (extending the time towards 400 ms resulted in an increase of the cBV-parameter, but did not change the conclusions).

- The mechanism of SCC cracking of Alloy 182 with SAM, STI and SP surfaces in BWR NWC is slip dissolution-oxidation mechanism.
- The high temperature re-passivation tests at 288 °C indicate a better passivation behaviour for the RS surface than SP surface. The CV and EIS data show that the SP surface has a clearly higher corrosion rate than RS surface.
- The results from CERT, constant load and electrochemical tests and the cross-sectional characterisations are well correlated.
- Peening induced surface defects/cracks, cracked/porous oxide layer and the residual stress relaxation (during dynamic loading) can explain the deteriorated SCC resistance of the SP surface finish.

CRediT authorship contribution statement

Study conception and design: Que, Saario and Ehrnstén. Acquisition of data: Que, Saario and Toivonen. Analysis and interpretation of data: Que, Saario and Toivonen. Drafting of manuscript: Que and Saario. Critical revision: Que, Saario, Toivonen and Ehrnstén.

Declaration of Competing Interest

The authors declare that they have no known competing financial interests or personal relationships that could have appeared to influence the work reported in this paper.

Data Availability

The data that support the findings of this study are available from the corresponding author upon reasonable request.

Acknowledgements

References

[1] S. Hwang, Review of PWSCC and mitigation management strategies of Alloy 600 materials of PWRs, J. Nucl. Mater. 443 (2013) 321–330.
[2] T. Shoji, Progress in the mechanistic understanding of BWR SCC and its implication to prediction of SCC growth behavior in plants, in: Proceedings of the 11th International Symposium on Environmental Degradation of Materials in Nuclear Power Systems-Water Reactors, Stevenson, Washington, USA, 2003.
[3] P. Scott, C. Benhamou, An overview of recent observations and interpretations of IGSCC in nickel base alloys in PWR primary water, in: Proceedings of the 10th International Symposium on Environmental Degradation of Materials in Nuclear Power Systems-Water Reactors, 2001.
[4] P. Andresen, P. Emigh, M. Morra, J. Hickling, Effects of PWR primary water chemistry and deaerated water on SCC, in: Proceedings of the 12th International Conference on Environmental Degradation of Materials in Nuclear Power Systems - Water Reactors, Snowbird, USA, 2005.
[5] J. Park, S. Yoo, J. Kim, C. Bahn, Development of probabilistic primary water stress corrosion cracking initiation model for alloy 182 welds considering thermal aging and cold work effects, Nucl. Eng. Technol. 53 (6) (2021) 1909–1923.
[6] D. Féron, C. Guerre, E. Herms, P. Laghoutaris, 9 – Stress corrosion cracking of Alloy 600: overviews and experimental techniques. Stress Corrosion Cracking of Nickel Based Alloys in Water-cooled Nuclear Reactors, Woodhead Publishing, 2016, pp. 325–353.
[7] Materials Reliability Program: GE Experience Report on Cracking in Alloy 182 (MRP-57): BWR Alloy 182 Stress Corrosion Cracking, EPRI Report, 2001.
[8] R. Staehle, Historical views on stress corrosion cracking of nickel-based alloys: the Coriou effect. Stress Corrosion Cracking of Nickel-based Alloys in Water-Cooled Nuclear Reactors, Woodhead Publishing, 2016, pp. 3–131.
[9] L. Chang, M.G. Burke, F. Scenini, Stress corrosion crack initiation in machined type 316L austenitic stainless steel in simulated pressurized water reactor primary water, Corros. Sci. 138 (2018) 54–65.
[10] L. Dong, X. Zhang, Y. Han, Q. Peng, P. Deng, Effect of surface treatments on microstructure and stress corrosion cracking behavior of 308L weld metal in a primary pressurized water reactor environment, Corros. Sci. 166 (108465) (2020), 108465.
[11] G. Dolores, J. Francisco, Environmentally-assisted cracking of nickel-base alloys in light water. Nuclear Corrosion: Research, Progress and Challenges, Woodhead Publishing, 2020, pp. 89–118.
[12] Z. Shen, K. Chen, D. Tweddle, G. He, K. Arioka, S. Lozano-Perez, Characterization of the crack initiation and propagation in Alloy 600 with a cold-worked surface, Corros. Sci. 152 (2019) 82–92.
[13] Y. Han, E. Han, Q. Peng, W. Ke, Effects of electropolishing on corrosion and stress corrosion cracking of Alloy 182 in high temperature water, Corros. Sci. 121 (2017) 1–10.
[14] Z. Zhai, M. Toloczko, M. Olszta, S. Bruemmer, Stress corrosion crack initiation of alloy 600 in PWR primary water, Corros. Sci. 123 (2017) 76–87.
[15] M. Mendonça, R.-W. Bosch, W. Renterghem, M. Vankeerberghen, C. Figueiredo, Effect of temperature and dissolved hydrogen on oxide films formed on Ni and Alloy 182 in simulated PWR water, J. Nucl. Mater. 477 (2016) 280–291.
[16] Z. Que, L. Volpe, A. Toivonen, G. Burke, F. Scenini, U. Ehrnstén, Effects of surface treatments on environmentally-assisted cracking susceptibility of Alloy 182 in BWR environment, Corros. Sci. 188 (109555) (2021), 109555.
[17] V. Raja, T. Shoji, Stress Corrosion Cracking Theory and Practice, Woodhead Publishing, 2011.

[18] T. Ahn, Long-term initiation time for stress-corrosion cracking of alloy 600 with implications in stainless steel: review and analysis for nuclear application, Prog. Nucl. Energy 137 (103760) (2021), 103760.

[19] R. Rebak, 7 – Stress corrosion cracking (SCC) of nickel-based alloys. Stress Corrosion Cracking Theory and Practice, Woodhead Publishing, 2011, pp. 273–306.

[20] F. Ford, Quantitative prediction of environmentally assisted cracking, Corrosion 52 (1996) 375–395.

[21] P. Scott, An overview of internal oxidation as a possible explanation of intergranular stress corrosion cracking of alloy 600 in PWRs, in: Proceedings of the International Symposium on Environmental Degradation of Materials in Nuclear Power Systems-Water Reactors, 1999.

[22] Z. Li, Y. Lu, X. Wang, Modeling of stress corrosion cracking growth rates for key structural materials of nuclear power plant, J. Mater. Sci. 55 (2020) 439–463.

[23] K. Chen, J. Wang, H. Su, L. Zhang, Investigation on the stress corrosion crack initiation and propagation behavior of Alloy 600 in high-temperature water, Corrosion 74 (12) (2018) 1395–1405.

[24] J. Bai, S. Ritter, H.-P. Seifert, S. Virtanen, Using tapered specimens to study the effect of hydrogen and surface finish on SCC initiation in Alloy 182 under boiling water reactor conditions, Corros. Eng. Sci. Technol. 52 (8) (2017) 558–566.

[25] R. Bosch, S. Ritter, M. Herbst, R. Kilian, M.G. Burke, Stress corrosion crack initiation testing with tapered specimens in high-temperature water – results of a collaborative research project, Corros. Eng. Sci. Technol. (2020).

[26] R. Basan, M. Franulović, I. Prebil, R. Kunc, Study on Ramberg-Osgood and Chaboche models for 42CrMo4 steel and some approximations, J. Constr. Steel Res. 136 (2017) 65–74.

[27] E. Richey, D. Morton, M. Schurman, SCC initiation testing of nickel-based alloys using in-situ monitored uniaxial tensile specimens, in: Proceedings of the 12th International Conference on the Environmental Degradation of Materials in Nuclear Power Systems – Water Reactors, Salt Lake City, Utah, USA, 2005.

[28] P. Andresen, J. Hickling, A. Ahluwalia, J. Wilson, Effect of H2 on mitigation of PWSCC in nickel alloys, in: Proceedings of the International Workshop on Optimization of Dissolved Hydrogen Content in PWR Primary Coolant, Sendai, Japan, 2007.

[29] R. Etien, E. Richey, D. Morton, J. Eager, SCC initiation testing of alloy 600 in high temperature water, in: Proceedings of the 15th International Conference on Environmental Degradation of Materials in Nuclear Power Systems – Water Reactors, 2011.

[30] K. Sipilä, M. Bojinov, E. Jäppinen, W. Mayinger, T. Saario, M. Selektor, Localized corrosion of pressure vessel steel in a boiling water reactor cladding flaw: modeling of electrochemical conditions and dedicated experiments, Electrochim. Acta 241 (2017) 10–27.

[31] Z. Que, C. Huotilainen, T. Seppänen, J. Lydman, U. Ehrnstén, Effect of machining on near surface microstructure and observation of martensite at the fatigue crack tip in PWR environment of 304L stainless steel, J. Nucl. Mater. 558 (153399) (2022), 153399.

[32] X. Wang, Z. Li, Y. Bai, X. Cao, T. Liu, Y. Lu, T. Shoji, Size effect of scratches on the degradation behavior of alloy 690TT in high temperature caustic solution, Corros. Sci. 182 (109314) (2021), 109314.

[33] C. Figueiredo, R.-W. Bosch, M. Vankeerberghen, Electrochemical investigation of oxide films formed on nickel alloys 182, 600 and 52 in high temperature water, Electrochim. Acta 56 (2011) 7871–7879.

[34] Z. Wang, Y. Takeda, Amorphization and structural modification of the oxide film of Ni-based alloy by in-situ H charging in high temperature high pressure water environment, Corros. Sci. 166 (108474) (2020), 108474.

[35] J. Panter, B. Viguier, J.-M. Cloue, M. Foucault, P. Combrade, E. Andrieu, Influence of oxide films on primary water stress corrosion cracking initiation of alloy 600, J. Nucl. Mater. 348 (2006) 213–221.

[36] K. Chen, Z. Shen, A study on the surface and crack tip oxidation of alloy 600 through high resolution characterization, Corros. Sci. 169 (108616) (2020), 108616.

[37] N. Saravanan, P. Karamched, J. Liu, C. Rainasse, F. Scenini, S. Lozano-Perez, Using local GND density to study SCC initiation, Ultramicroscopy 217 (113054) (2020), 113054.

[38] P. Lin, G. Palumbo, U. Erb, Influence of grain-boundary-character-distribution on sensitization and intergranular corrosion of Alloy-600, Scr. Metall. Mater. 33 (9) (1995) 1387–1392.

[39] W. Kuang, G. Was, The effect of grain boundary structure on the intergranular degradation behavior of solution annealed alloy 690 in high temperature, hydrogenated water, Acta Mater. 182 (120–130) (2020) 120–130.

[40] K. Arioka, Role of cavity formation on long-term stress corrosion cracking initiation: a review, Corrosion 76 (2) (2020) 142–175.

[41] A. Hojná, Environmentally assisted cracking initiation in high-temperature water, Metals vol. 11 (199) (2021) 199.

[42] S. Fyfitch, 5.04 Corrosion and stress corrosion cracking of Ni-base alloys. Comprehensive Nuclear Materials, Elsevier, 2012, pp. 69–92.

[43] MRP-267, Revision 1: Materials Reliability Program: Technical Basis for Primary Water Stress Corrosion Cracking Mitigation by Surface Stress Improvement, EPRI Report, 2012.

[44] J. Bourisier, D. Desjardins, F. Vaillant, The influence of the strain-rate on the stress corrosion cracking of alloy 600 in high temperature primary water, Corros. Sci. 37 (3) (1995) 493–508.

[45] C. Duhamel, J. Caballero, T. Couvant, J. Crépin, F. Gaslain, C. Guerre, H. Le, M. Wehbi, Intergranular oxidation of nickel-base alloys: potentialities of focused ion beam tomography, Oxid. Met 88 (2017) 447–457.

[46] R. Sundar, P. Ganesh, K. Ram, G. Ragvendra, B. Pant, K. Vivekanand, K. Ranganathan, K. Rakesh, K. Bindra, Laser shock peening and its applications: a review, Lasers Manuf. Mater. Process. 6 (2019) 424–463.

[47] F. Bernard, V. Rao, H.-S. Kwon, A study on the repassivation kinetics and SCC behavior of duplex stainless steel in chloride solution, J. Electrochem. Soc. 152 (10) (2005) B415.

[48] S. Nishikawa, K. Ooi, M. Takahashi, T. Furukawa, Influence of shot peening and thermal ageing treatment on resistance to intergranular corrosion in shielded metal arc weld metal for type 600 nickel base alloy, Weld. Int. 31 (11) (2017) 837–845.

[49] T.-K. Yeh, G.-R. Huang, M.-Y. Wang, C.-H. Tsai, Stress corrosion cracking in dissimilar metal welds with 304L stainless steel and Alloy 82 in high temperature water, Prog. Nucl. Energy 63 (2013) 7–11.

[50] D. Buchanan, R. John, Residual stress redistribution in shot peened samples subject to mechanical loading, Mater. Sci. Eng. A 615 (2014) 70–78.

[51] J. Boursier, F. Vaillant, P. Saulay, Y. Brechet, G. Zacharie, Effect of the strain rate on the stress corrosion cracking in high temperature primary water: comparison between the Alloys 690 and 600, in: Proceedings of the 11th International Conference on Environmental Degradation of Materials In Nuclear Systems, 2003.